Construction of iodine vacancy-rich BiOI/Ag@AgI Z-scheme heterojunction photocatalysts for visible-light-driven tetracycline degradation: Transformation pathways and mechanism insight

Yang Yang[a,1], Zhuotong Zeng[b,1], Chen Zhang[a,1], Danlian Huang[a,1], Guangming Zeng[a,b,*], Rong Xiao[b,*], Cui Lai[a], Chengyun Zhou[a], Hai Guo[a], Wenjing Xue[a], Min Cheng[a], Wenjun Wang[a], Jiajia Wang[a]
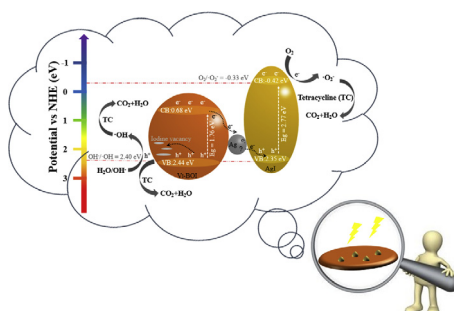
[a] College of Environmental Science and Engineering, Hunan University and Key Laboratory of Environmental Biology and Pollution Control (Hunan University), Ministry of Education, Changsha 410082, PR China
[b] Department of Dermatology, Second Xiangya Hospital, Central South University, Changsha 410011, PR China

HIGHLIGHTS

- A novel Z-scheme iodine vacancy-rich BiOI/Ag@AgI photocatalyst was constructed.
- An amazing photocatalytic activity for the degradation of TC refractory antibiotics.
- Three possible degradation pathways for TC was illustrated.
- A plausible iodine vacancies assisted Z-scheme photocatalytic mechanism was proposed.

GRAPHICAL ABSTRACT

ABSTRACT

Constructing highly efficient visible-light-driven (VLD) photocatalysts for organic pollutants degradation has been unearthed as a promising and green strategy on environmental remediation. In this study, a novel iodine vacancy-rich BiOI/Ag@AgI (Ag@AgI/V_I-BOI) Z-scheme heterojunction photocatalyst was successfully constructed, where Ag@AgI nanoparticles in-situ grown on the surface of defective BiOI nanosheets. The morphology and structure, optical, photoluminescence, and photo-electrochemical properties of the photocatalysts were detailedly characterized. Tetracycline (TC) as a refractory antibiotic was chosen as target pollutant to evaluated the photocatalytic performance of the Ag@AgI/V_I-BOI photocatalyst. The Z-scheme Ag@AgI/V_I-BOI photocatalyst possessed significantly boosted photocatalytic efficiency for the degradation of TC under visible light irradiation (λ > 420 nm), which was better than that of BiOI, V_I-BOI, and Ag@AgI. The impacts of photocatalyst dosages, initial TC concentrations, inorganic anions and light irradiation conditions on TC degradation were also explored. Importantly, the intermediates and possible decomposition pathways of TC were illustrated through liquid chromatography coupled with tandem mass spectrometry (LC-MS/MS) and three-dimensional excitation-emission matrix fluorescence spectroscopy (3D EEMs) analysis. The enhanced photocatalytic activity of the Ag@AgI/V_I-BOI is attributed to the synergetic effect among iodine vacancies, AgI/V_I-BOI heterojunction and metallic Ag^0. Additionally, the photocatalyst presented high recyclability and stability. This

work can afford a new reference for fabricating photocatalyst with synergistic effect and amazing capacity for practical wastewater treatment.

1. Introduction

With the rapid growth of industrialization and urbanization, the environmental pollution is becoming an overwhelming problem across the world [1–7]. Among of all problems, water pollution is one of the most urgent issues to be solved, especially for the antibiotics owing to their potential threat to the survival of aquatic animals and plants or even human health [8–12]. As a typical antibiotic, tetracycline (TC) is widely distributed in water bodies and hardly be decomposed naturally due to its antibacterial nature and chemical stability. Moreover, conventional treatment methods, including physical adsorption [13–16], chemical oxidation [17–20] and biological filtration [21–23], are limited by complex process, expensive infrastructure and possible secondary pollution. Therefore, developing an efficient, convenient and "green" technique for TC removal has become a critical and pressing task.

Recently, semiconductor photocatalysis technique which can utilize solar light to solve energy and environmental issues has aroused widespread concerns, owing to its high-performance, energy-efficient and economic properties [24–27]. Among the numerous photocatalysts, bismuth oxyiodide (BiOI) has been widely investigated because of its suitable band gap and desirable photocatalytic performance under visible light irradiation [28,29]. However, as for pristine BiOI, the relative photocatalytic activity still needs to be enhanced due to its fast recombination rate of photo-generated electron-hole pairs [30]. Thus, the appropriate modification is necessary to further promote the photocatalytic activity of BiOI. Engineering vacancies in the lattices of photocatalysts have been proved to be effective to improve the photocatalytic activity of photocatalysts, as vacancies can not only facilitate the separation of photo-generated electron-hole pairs, but promote the transfer of photo-induced charges [31–33]. In previous reports [34,35], it has been found that the iodine vacancy-rich BiOI possessed much better photocatalytic performance than that of stoichiometric BiOI since iodine vacancy played an important role in the regulation of the charge separation and transportation. Moreover, for BiOI, iodine vacancies are easily formed as a result of its unique layered structures, which are composed of $[Bi_2O_2]^{2+}$ slabs and inserted negative double iodine slabs with weak van der Waals interactions along the *c*-axis [36]. Accordingly, it is feasible to prepare defective BiOI modified with iodine vacancies for promoting the photocatalytic performance.

Although vacancies display significant potential for the enhancement of photocatalytic activity, there is still room for improvement. Previous reports demonstrated that the construction of heterojunction is an advisable approach to designing high-efficient photocatalysts [28,29]. Among the heterojunction photocatalysts, the Z-scheme photocatalytic system has outstanding ability to inhibit the recombination of photo-generated electron-hole pairs [37–40]. Therefore, finding a suitable photocatalysts to construct a Z-scheme system with defective BiOI is a promising way. Recently, much attention has been drawn to Ag@AgX (X = Cl, Br, I)-based composite photocatalysts due to the surface plasmon resonance effect and excellent capability to transfer electrons of metallic Ag^0. For example, Ag@AgBr/PbBiO₂Br [40], Ag@AgX/BiOX (X = Cl, Br) [41], Ag@AgCl/CeO₂ [42], Ag@AgX/RGOs (X = Cl, Br, I; RGO = reduced graphene oxide) [43] and Ag@AgI/Bi-BiOI [44] all possessed increased VLD photocatalytic degradation and disinfection activity. However, studies on Ag@AgI nanoparticles modified iodine vacancy-rich BiOI nanosheets have never been investigated. Also, a visible light photocatalytic TC degradation with this Ag@AgI/V_I-BOI nanocomposite has not been reported.

In this study, a novel photocatalyst which was composed of

defective BiOI nanosheets (iodine vacancy) and in-situ Ag@AgI nanoparticles (Ag@AgI/V_I-BOI) was successfully synthesized. The photocatalytic performance of the photocatalysts was evaluated through the TC removal efficiency under visible light irradiation. Moreover, the possible decomposition pathways of the degradation process were illustrated through the liquid chromatography coupled with tandem mass spectrometry (LC/MS-MS) and three-dimensional excitation-emission matrix fluorescence spectroscopy (3D EEMs) analysis. It was demonstrated that the synergetic effect among iodine vacancies, AgI/V_I-BOI heterojunction and metallic Ag^0 should contribute to the enhanced photocatalytic activity towards TC degradation. A possible iodine vacancies assisted Z-scheme photocatalytic mechanism was proposed for better understanding the intrinsic reaction procedures by Ag@AgI/V_I-BOI photocatalyst.

2. Materials and methods

2.1. Materials

Bismuth nitrate pentahydrate (Bi(NO₃)₃·5H₂O), potassium iodide (KI), silver nitrate (AgNO₃), ethylene glycol (EG) and tetracycline (TC) were purchased from Sinopharm Chemical Reagent Co. Ltd (Shanghai, China). All chemicals were from commercial sources and used without any further purification. De-ionized water (18.25 MΩ cm specific resistance) was used in all the experiments.

2.2. Preparation of V_I-BOI nanosheets

The defective BiOI nanosheets with iodine vacancies (V_I-BOI) were synthesized by a facile EG-assisted hydrolysis method and further calcination treatment. Typically, Bi(NO₃)₃·5H₂O (2 mmol) and KI (2 mmol) were firstly dissolved into 50 mL of EG and 50 mL of de-ionized water under ultrasonic treatment, respectively. Then, Bi(NO₃)₃·5H₂O solution was dropwise added into KI solution resulting in brick-red precipitate and kept stirring at room temperature for 3 h. The precipitate was separated via filtration, washed three times with de-ionized water and ethanol, and dried at 60 °C for 12 h. Finally, the BiOI nanosheets were heat treated at 340 °C for 2 h in air at a heating rate of 3 °C min⁻¹ and cooled to room temperature naturally.

2.3. Preparation of Ag@AgI/V_I-BOI nanocomposite

The Ag@AgI/V_I-BOI nanocomposite was prepared via an in situ ion-exchange process and a photo-deposition route. Briefly, 0.30 g of V_I-BOI sample was firstly dispersed into 100 mL de-ionized water containing a certain amount of AgNO₃ under ultrasonic processing, and vigorously stirred in dark for 12 h. Through the in situ ion-exchange process, AgI nanoparticles formed on the surface of V_I-BOI nanosheets, while the generated BiO⁺ ions dissolved in the solvent (V_I-BOI + Ag⁺ → AgI ↓ + BiO⁺) [45]. Next, the suspension was irradiated by a 300 W xenon lamp equipped with a UV cutoff filter (λ > 420 nm) for 30 min so that the Ag⁺ species on the surface of AgI/V_I-BOI were reduced to Ag^0. Then the resulting precipitate was filtered, washed with de-ionized water and ethanol repeatedly, and dried at 60 °C overnight. The initial mass ratios of AgNO₃ to V_I-BOI were regulated 2%, 5%, 10% and 20% meanwhile the corresponding products were denoted as 2%, 5%, 10% and 20%-nanocomposite, respectively. For comparison, an Ag@AgI sample was synthesized through direct precipitation of AgNO₃ and KI aqueous solution followed by visible light irradiation reduction for 30 min. Additionally, a mechanically physically mixed Ag@AgI and V_I-BOI sample

(AgNO$_3$/V$_I$-BOI mass ratio = 10%, denoted as Mix) was prepared.

2.4. Characterization

The crystal structures of the samples were determined by X-ray diffraction (XRD, XRD-6100, Shimadzu) with Cu Kα radiation, operating at a 2θ range from 10° to 80°. X-ray photoelectron spectroscopy (XPS) was analyzed on a spectrometer (Escalab 250Xi, Thermo) using an Al Kα X-ray source (1486.6 eV). The mass ratio of bismuth and iodine was measured on an X-ray fluorescence spectrometer (XRF, XRF-1800, Shimadzu). The morphologies were observed by using a field-emission scanning electron microscopy (FESEM, SU8010, Hitachi) with energy-disperse X-ray spectroscopy (EDS). Transmission electron microscopy (TEM) and high resolution TEM (HRTEM) images were acquired using a transmission electron microscope (TEM, Tecnai G2 F20, FEI) at an accelerating voltage of 200 kV. The Brunauer-Emmett-Teller (BET) specific surface areas were measured on a surface area analyzer (Belsorp-miniII, BEL) by nitrogen adsorption–desorption. The ultra-violet visible diffused reflectance spectra (UV–vis DRS) were collected on an UV–vis spectrophotometer (Cary 300, Varian) in the wavelength range from 300 nm to 800 nm with BaSO$_4$ as the reference. The total organic carbon (TOC) assays were conducted on Shimadzu TOC-VCPH analyzer. The three-dimensional excitation-emission matrix fluorescence spectra (3D EEMs) and the photoluminescence (PL) spectra were acquired on a fluorescence spectrophotometer (LS-55, PerkinElmer). The electron spin response (ESR) signals of free radical were examined on a spectrometer (JES-FA200, JEOL) under visible light irradiation (λ > 420 nm) using 5,5-dimethyl-1-pyrroline N-oxide (DMPO) as spin-trapped reagent.

2.5. Photocatalytic activity tests

The photocatalytic activities of the nanocomposites were evaluated by the degradation of TC under visible light irradiation (λ > 420 nm). Visible illumination was obtained by a 300 W Xe lamp (CEL-HXF300, Ceaulight) equipped with a 420 nm cutoff filter. Typically, 30 mg of the sample was dispersed into a 100 mL of 20 mg L^{-1} TC aqueous solution. Prior to irradiation, the suspensions were fiercely magnetically stirred for 30 min in the dark to reach the adsorption–desorption equilibrium. Then, visible light irradiation was carried out. At given reaction time intervals, 4 mL of the reaction suspensions were taken out and centrifuged to remove the photocatalyst powder, and the concentration of TC was monitored by an UV–vis spectrophotometer (UV-2700, Shimadzu) through checking its characteristic absorbance at 357 nm.

The degradation efficiency (DE, %) was calculated by the following equation:

$$DE\ (\%) = \frac{C_0 - C_t}{C_0} \times 100\% \tag{1}$$

where C_O is the initial concentration of TC, and C_t is the TC concentration at time t.

2.6. Degradation intermediates identification

The degradation intermediates of TC were identified by a LC-MS/MS system (1290/6460 Triple Quad, Agilent) equipped with a Kromasil C18 column (250 × 4.6 mm, 5 μm). The elution was performed via 0.1% (v/v) of formic acid aqueous solution (A) and acetonitrile (B) at a flow rate of 0.2 mL min^{-1}. The injection volume was 2 μL, and the column temperature was 30 °C. Linear gradient elution as follows: the initial 90% A was reduced to 10% A over 10 min and kept 4 min. Then the mobile phase A returned to 90% in 1 min and maintained 1 min. MS was conducted in the positive ion mode using an electrospray ionization (ESI) source under the following conditions: capillary voltage, 4.0 kV; gas (N$_2$) flow rate, 11 L min^{-1}; gas temperature, 300 °C; nebulization pressure, 15 psi. MS was scanned by mass range from 200 to 600 m/z.

2.7. Photo-electrochemical measurements

The transient photocurrent response measurements were conducted on a conventional three-electrode model on a CHI 760E workstation. A Pt electrode and a saturated calomel electrode (SCE) were used as counter electrode and reference electrode, respectively. 0.2 M Na$_2$SO$_4$ was used as electrolyte and a 300 W Xe lamp equipped with a 420 nm cutoff filter was utilized to provide visible light. The working electrode was fabricated through coating photocatalyst on a fluorine-doped tin oxide (FTO) glass. Briefly, 10 mg of the photocatalyst was dispersed into 100 μL of 25% polyvinyl alcohol (PVA) solution to get slurry. After 1 h of ultrasonication, the slurry was dropped onto a 1 cm^2 effective working area of the 1 cm × 2 cm FTO glass which has been cleaned by acetone, ethanol and de-ionized water, respectively. The electro-chemical impedance spectroscopy (EIS) was tested based on the above workstation and three-electrode system under a 5 mV amplitude of alternating voltage in the frequency range of 10^5–10^{-1} Hz.

3. Result and discussion

3.1. Characterization of the obtained samples

Fig. 1 shows the XRD patterns of BiOI, V$_I$-BOI, 10% Ag@AgI/V$_I$-BOI and Ag@AgI, respectively. For the pure BiOI and Ag@AgI, characteristic diffraction peaks can be easily indexed to the BiOI of tetragonal phase (JCPDS NO. 10-0445) and the AgI of hexagonal phase (JCPDS NO. 09-0374), respectively. Compared to pristine BiOI, the diffraction peak (1 0 2) of V$_I$-BOI shifts slightly to the lower diffraction angle and other peaks ((1 0 3) and (1 1 4)) nearly disappear. It is mainly attributed to the volatilization of iodine element on calcination treatment resulting in the excess bismuth and oxygen in the [Bi$_2$O$_2$]$^{2+}$ lattice, which can bring about expansion and distortion for BiOI crystal structure [34,35]. Moreover, when Ag@AgI was involved in the V$_I$-BOI, a distinct change in XRD pattern was observed. It is noted that diffraction peaks of AgI ((1 0 0), (0 0 2), (1 1 0) and (1 1 2)) exist in the pattern of 10% Ag@AgI/V$_I$-BOI. The diffraction peak (1 0 2) of 10% Ag@AgI/V$_I$-BOI has a little expansion compared with V$_I$-BOI due to the iodine element on AgI is derived from V$_I$-BOI via in situ ion-exchange process [44]. Notably, there is no obvious diffraction peaks of Ag^0 emerged in the patterns because of high dispersity and low content of Ag^0 [46]. From XRD analysis, it is found that 10% Ag@AgI/V$_I$-BOI nanocomposite was successfully fabricated. And no other peaks originated from impurities appear, indicating good crystalline of the photocatalysts.
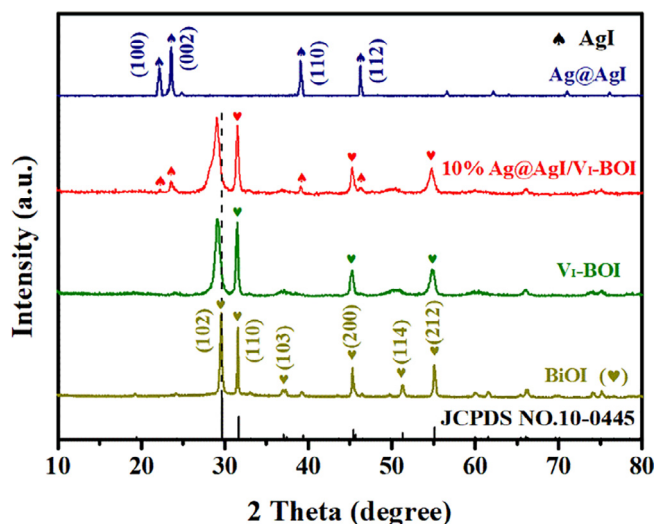

Fig. 1. XRD patterns of pure BiOI, V$_I$-BOI, Ag@AgI and 10% Ag@AgI/V$_I$-BOI samples.

The surface chemical compositions and chemical states of surface elements for BiOI, V_I-BOI and 10% Ag@AgI/V_I-BOI were analyzed by XPS. As displayed in Fig. 2a, three elements of Bi, O and I can be easily found in the survey XPS spectra of the BiOI and V_I-BOI while four elements of Bi, O, I and Ag can be detected in the 10% Ag@AgI/V_I-BOI, which are in coincidence with their chemical compositions. Meanwhile, the high-resolution XPS spectra of Bi 4f, O 1s, I 3d and Ag 3d are shown in Fig. 2b–e, respectively. As presented in Fig. 2b, the two peaks of BiOI situated at 159.08 eV and 164.28 eV belong to Bi $4f_{7/2}$ and Bi $4f_{5/2}$, indicating that Bi exists as Bi^{3+} in the BiOI [47]. The binding energy of Bi 4f in V_I-BOI and 10% Ag@AgI/V_I-BOI upward shift slightly compared with BiOI. This is because that O atoms replace some I atoms and the formation of AgI consumes a part of I atoms, which can increase the interaction between Bi^{3+} and O^{2-} [34,48]. Fig. 2c illustrates the high-

resolution spectra of O 1s, the binding energy of O 1s for BiOI, V_I-BOI and 10% Ag@AgI/V_I-BOI gradually raise due to the enhanced interaction between Bi^{3+} and O^{2-}. Moreover, the expansion of the peaks is mainly ascribed to the chemisorbed oxygen and the surface hydroxyl groups [47]. As for I 3d (Fig. 2d), the peaks of BiOI at 619.48 eV and 630.88 eV are assigned to I $3d_{5/2}$ and I $3d_{3/2}$, respectively [29]. In comparison to BiOI, the binding energy of I 3d in V_I-BOI decrease slightly, which is in accordance with the results published in previous papers [35]. After involving Ag@AgI, the bind energy of I 3d for 10% Ag@AgI/V_I-BOI marginally increase, implying that I^- of V_I-BOI and 10% Ag@AgI/V_I-BOI are in different ambient chemical environment. In Fig. 2e, the Ag $3d_{5/2}$ and Ag $3d_{3/2}$ peaks of 10% Ag@AgI/V_I-BOI are deconvoluted into four characteristic peaks, where 368.34 and 368.68 eV refer to Ag $3d_{5/2}$ and the other two peaks (374.36 and
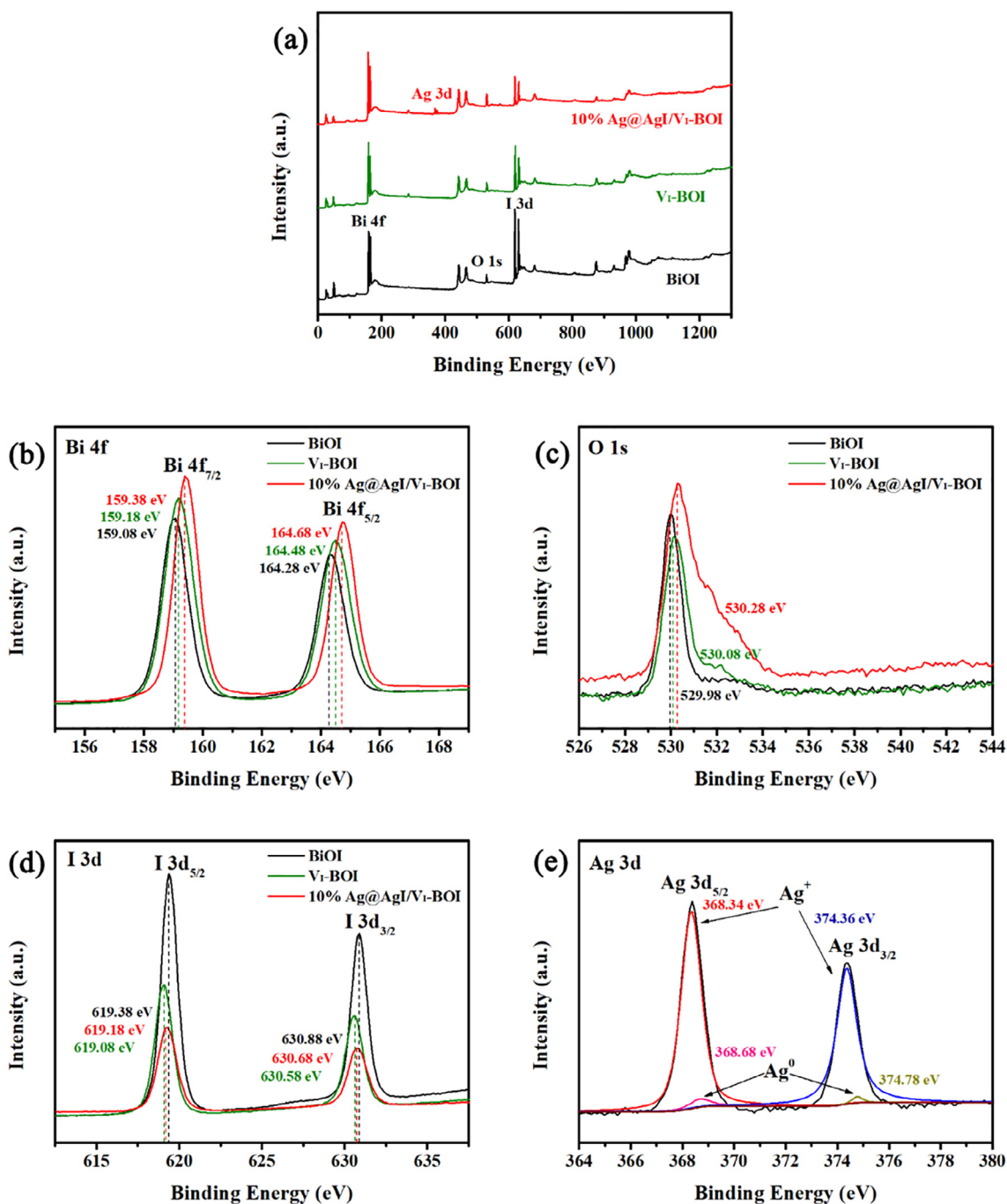

Fig. 2. XPS spectra of the BiOI, V_I-BOI and 10% Ag@AgI/V_I-BOI samples: (a) total survey, (b) Bi 4f, (c) O 1s, (d) I 3d, and (e) Ag 3d.

374.78 eV) are attributed to Ag $3d_{3/2}$, respectively. The two new peaks located at 368.68 and 374.78 eV are assigned to Ag^0 species [46]. In addition, XRF was utilized to measure the mass ratios of Bi and I in the samples [33]. As exhibited in Table S1, the atomic ratio of Bi/I increased from 1.06 for BiOI to 1.38 for V_I-BOI, indicating that some iodine atoms were escape and iodine vacancies were formed during calcination treatment. Therefore, the XPS and XRF results clearly demonstrate the presence of iodine vacancies and the successful preparation of Ag@AgI/V_I-BOI heterostructures.

The morphology and microstructure of BiOI, V_I-BOI, and 10% Ag@AgI/V_I-BOI were characterized by FESEM and the corresponding images are displayed in Figs. S1 and 3a and b. As depicted in Fig. S1, the BiOI and V_I-BOI all present as 3D hierarchical structure which is assembled with nanosheets. As for the 10% Ag@AgI/V_I-BOI (Fig. 3a and b), its surface expresses some difference compared with that of the V_I-BOI. From Fig. 3b, it can be observed that the Ag@AgI nanoparticles are tightly attached to the V_I-BOI nanosheets, demonstrating Ag@AgI is successfully introduced to V_I-BOI. Additionally, the SEM-EDS elemental mapping of 10% Ag@AgI/V_I-BOI shows the distribution status of the component elements. All four elements (Bi, O, I and Ag) are uniformly distributed throughout the whole nanocomposite as illustrated in Fig. S2.

Further detailed information about the morphology and microstructure of 10% Ag@AgI/V_I-BOI was obtained by utilizing TEM and HRTEM technique and the images are depicted in Fig. 3c and d. The TEM image (Fig. 3c) distinctly reveals that the Ag@AgI nanoparticles are uniformly distributed in the V_I-BOI, which is in accordance with the results presented in the SEM image. Moreover, the HRTEM image shown in Fig. 3d illustrates that three different lattice fringes of 0.283, 0.229 and 0.232 nm are observed in the photocatalysts. The fringe interval of 0.283 nm is in line with the interplanar spacing of (1 1 0) plane for tetragonal phase BiOI, while the fringe intervals of 0.229 and 0.232 nm are ascribed to the (1 1 0) plane of hexagonal phase AgI and (1 1 1) plane of face-centered cubic Ag, respectively [28,46,49]. The TEM and HRTEM images indicate the intimate attachments of Ag@AgI nanoparticles on V_I-BOI nanosheets.

Meanwhile, Fig. S3 exhibits the nitrogen adsorption–desorption isotherms of the BiOI, V_I-BOI and 10% Ag@AgI/V_I-BOI samples. All the isotherms belong to the classical type IV, implying the existence of mesopores [50]. The BET specific surface area (S_{BET}) and pore volume of the three samples are listed in Table S2. As collected in Table S2, the S_{BET} were measured to be 10.93, 11.34 and 11.41 $m^2 g^{-1}$ for BiOI, V_I-BOI and 10% Ag@AgI/V_I-BOI, while the pore volume of them were calculated to be 0.034, 0.070 and 0.081 $cm^3 g^{-1}$, respectively. Overall, the S_{BET} and pore volume of BiOI, V_I-BOI and 10% Ag@AgI/V_I-BOI increase in turn, which would adsorb more active species and reactants and provide more reaction sites for photocatalysis.
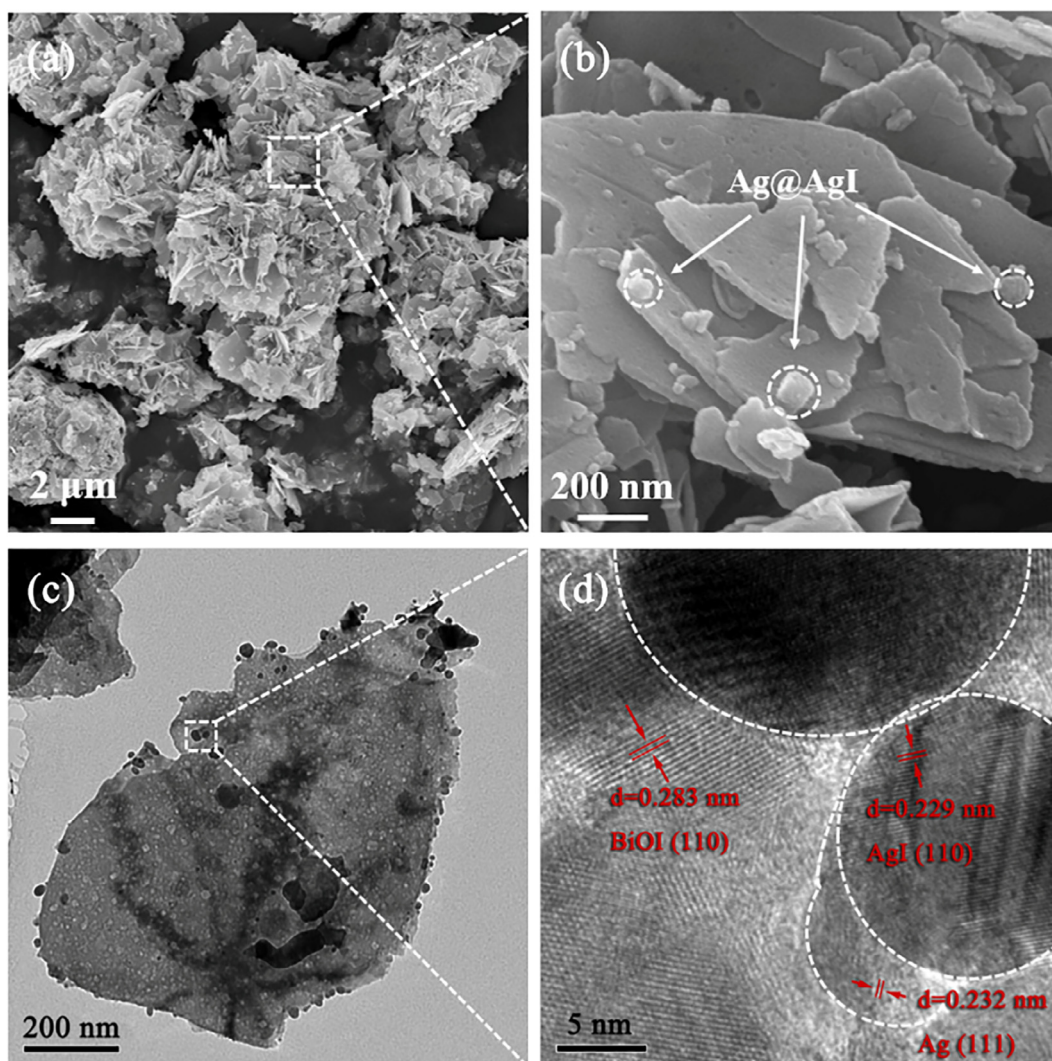

Fig. 3. (a and b) FESEM, (c) TEM, and (d) HRTEM images of 10% Ag@AgI/V_I-BOI.

3.2. Photocatalytic performance

The photocatalytic performance of Ag@AgI/V_I-BOI nanocomposite was assessed through the degradation of TC. Fig. 4a depicts a diagram of TC removal efficiency on photocatalysts with different components. Obviously, all the samples can adsorb TC to some degree in the darkness. As shown in Fig. S4, the adsorption capacity of BiOI, V_I-BOI and 10% Ag@AgI/V_I-BOI increased in turn due to the increased S_{BET} and pore volume. Therefore, more active species and reactants can be adsorbed and more reaction sites can be provided for photocatalysis. With the prolongation of irradiation time, the concentration of TC gradually reduced for the all samples. The degradation efficiency was only 29.26% for pure BiOI within 60 min visible light irradiation, while 60.86% of TC was degraded by V_I-BOI under the same condition. After coupling with appropriate amount of Ag@AgI, the TC degradation efficiency was improved significantly and 10% Ag@AgI/V_I-BOI presented the highest degradation efficiency of 86.40%. The time-dependent UV–vis spectra of TC on 10% Ag@AgI/V_I-BOI is displayed in Fig. 4b. As exhibited in Fig. 4b, the absorbance of TC decreased with the increase of reaction time. This prominent enhancement is due to the synergistic effect among iodine vacancies, AgI/V_I-BOI heterojunction and Z-scheme bridge metallic Ag^0, which can accelerate separation and slow recombination of the photo-generated electron-hole pairs and thus greatly promote the photocatalytic activity. In contrast, the single Ag@AgI can merely degrade 66.59% of TC. Notably, the photocatalytic activity of physically mixed Ag@AgI and V_I-BOI was much inferior than that of the 10% Ag@AgI/V_I-BOI nanocomposite, suggesting that the Ag@AgI and V_I-BOI on 10% Ag@AgI/V_I-BOI have formed interface chemical contact intimately. Furthermore, the plots of $-\ln(C_t/C_0)$ versus irradiation time (*t*) are discovered to be linear correlation as shown in Fig. 4c, indicating that the reaction follows a pseudo-first-
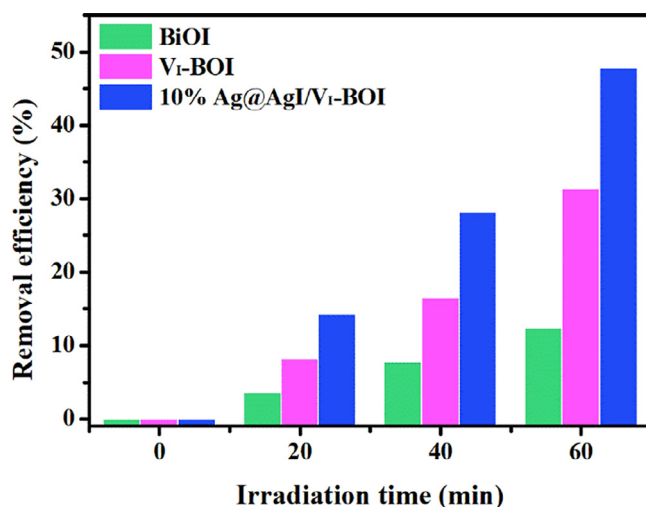

Fig. 5. The total organic carbon (TOC) removal efficiencies of the BiOI, V_I-BOI and 10% Ag@AgI/V_I-BOI.

order model. The apparent rate constants (*k*) are evaluated by the following equation and are illustrated in Fig. 4d [46]:

$$\ln\left(\frac{C_t}{C_0}\right) = -kt \tag{2}$$

where C_0 and C_t is the concentration of TC at time *0* and *t*, respectively. It can be clearly observed that the *k* value of 10% Ag@AgI/V_I-BOI (0.0317 min^{-1}) is largest from Fig. 4d, which is about 7.2 times and 2.3 times as that of BiOI (0.0044 min^{-1}) and V_I-BOI (0.014 min^{-1}),
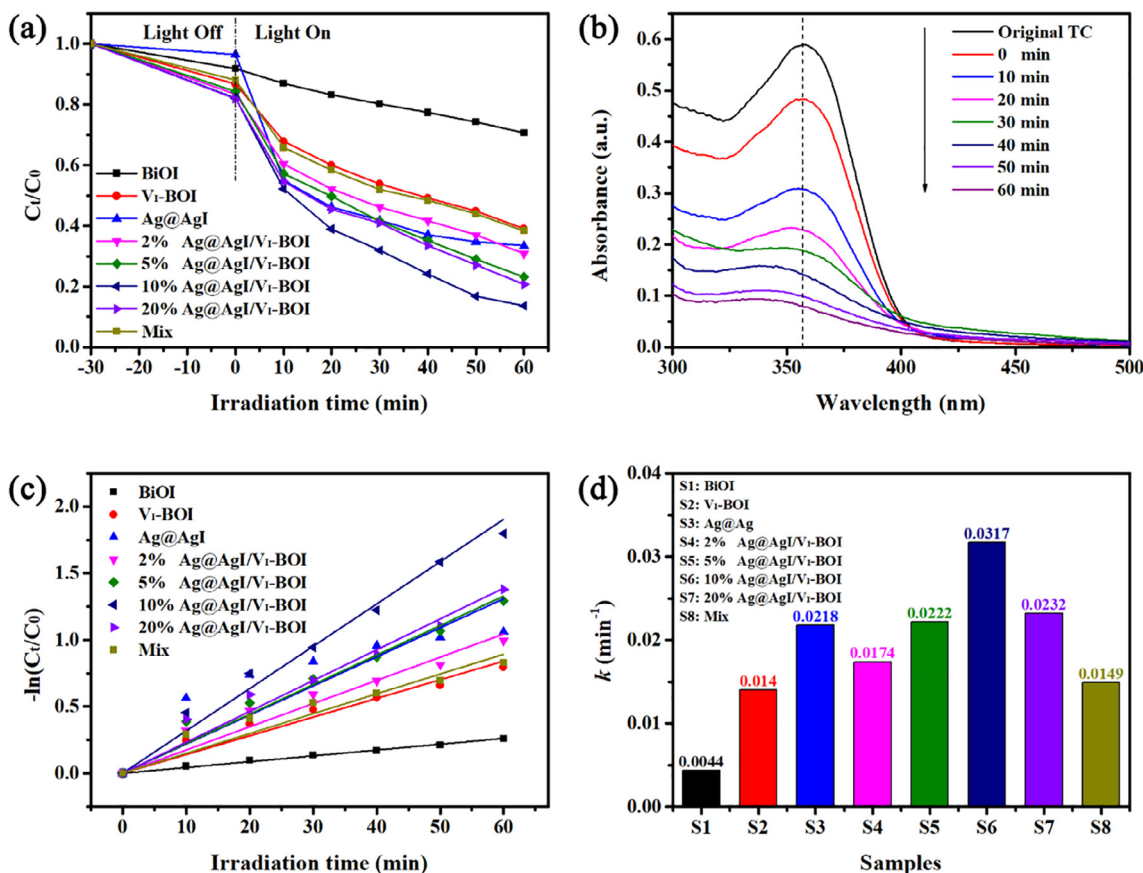

Fig. 4. (a) Photocatalytic degradation TC curves; (b) time-dependent UV–vis spectra of TC solution for 10% Ag@AgI/V_I-BOI sample; (c) kinetic curves of TC degradation; and (d) apparent rate constants for the degradation of TC.

respectively. Moreover, the removal efficiency of total organic carbon (TOC) was investigated to evaluate the mineralization ability of the photocatalysts. As illustrated in Fig. 5, the TOC removal efficiencies for the pristine BiOI, V_I-BOI and 10% Ag@AgI/V_I-BOI were 12.37%, 31.35% and 47.78%, respectively. The results mentioned above demonstrate that the 10% Ag@AgI/V_I-BOI nanocomposite not only possessed the best photocatalytic performance for the TC degradation but it also had excellent mineralization ability, and the enhanced photocatalytic activity can be ascribed to the synergetic effect among iodine vacancies, AgI/V_I-BOI heterojunction and Z-scheme bridge metallic Ag^0. Besides, in order to optimize reaction conditions in the practical applications, various conditions such as photocatalyst dosages, initial TC concentrations, presence of inorganic anions and light irradiation conditions for the impact of the TC degradation performances were investigated, as shown in Fig. 6.

3.2.1. The impact of photocatalyst dosages

In practical applications, the control of photocatalyst dosage is necessary as it can directly influence the cost and photocatalytic performance. As depicted in Fig. 6a, the TC was hardly degraded without the proposed photocatalyst, indicating the photolysis of TC is negligible under visible light irradiation. The degradation efficiencies of TC significantly increased from 66.35% to 86.40% along with the dosages of 10% Ag@AgI/V_I-BOI photocatalyst increased from $0.10\,g\,L^{-1}$ to $0.30\,g\,L^{-1}$. However, as the photocatalyst amount further increased, the TC degradation efficiency gradually decreased. The phenomenon is because the photons are a constant on a certain period of time when the visible light irradiation is stable. Hence there is an optimal amount of photocatalyst which can make the maximum use of photo energy [51]. When the photocatalyst dosage is less than the optimal amount, the

photons utilization rate is insufficient and thus results in the low TC degradation efficiency. With the increase of photocatalyst dosage more than the optimal amount, the photocatalytic activity is inhibited because of the increased turbidity and decreased transmissivity of solution. Thus, the photocatalyst dosage of $0.30\,g\,L^{-1}$ is chosen as the optimal dosage for the experiments.

3.2.2. The impact of initial TC concentrations

Actually, the concentration of TC varies extensively in the natural environment. It is essential to discuss the impact of initial TC concentration on the photocatalytic performance of the photocatalyst. Fig. 6b displays the degradation efficiency of TC for 10% Ag@AgI/V_I-BOI nanocomposite on different initial concentrations of TC. Obviously, it can be seen that the initial TC concentration had a distinct influence on the photocatalytic degradation reaction, and the removal efficiencies of TC declined from 86.40% to 47.12% when the initial TC concentrations increased from $20\,mg\,L^{-1}$ to $60\,mg\,L^{-1}$, respectively. This is due to the depressed light penetration and accumulated intermediates. Specifically, the increase of initial TC concentration restrains the penetration of light to aqueous solution, resulting in the reduction of available photons. Besides, the increased intermediates of TC aggravate the adsorption competition between TC molecules and intermediates and lead to the inhibition of TC degradation [50]. Herein, the initial TC concentration of $20\,mg\,L^{-1}$ is picked out for the investigations.

3.2.3. The impact of inorganic anions

Various inorganic anions in actual water bodies affect the treatment of pollutants. To investigate the influence of inorganic anions for the TC degradation by 10% Ag@AgI/V_I-BOI photocatalyst, the sodium salts of
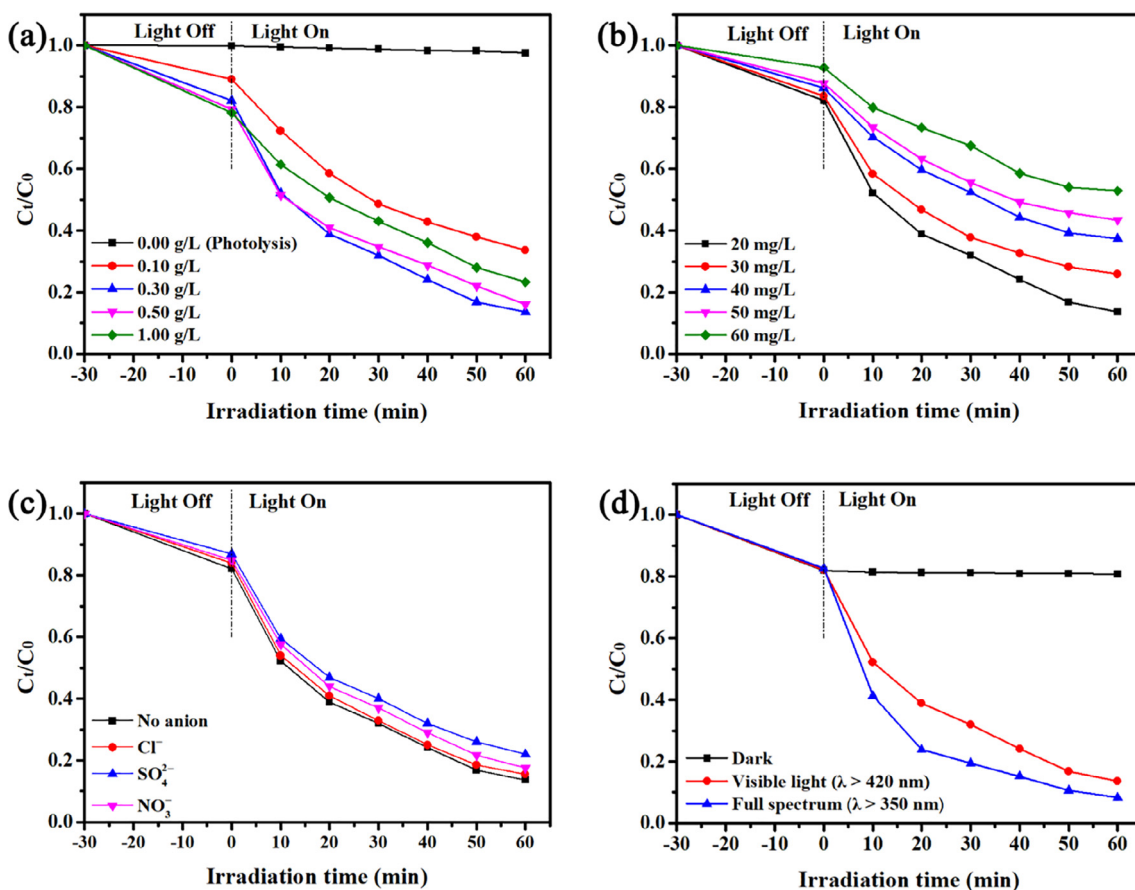

Fig. 6. The impact of (a) photocatalyst dosages, (b) initial TC concentrations, (c) inorganic anions, and (d) light irradiation conditions on the TC photocatalytic degradation efficiency in the presence of 10% Ag@AgI/V_I-BOI.

Cl$^-$, SO$_4^{2-}$, NO$_3^-$ at a concentration of 0.05 M were adopted because Na$^+$ exhibit an inapparent influence for the photocatalytic degradation of TC [28]. As depicted in Fig. 6c, the presence of Cl$^-$ restrained the TC degradation slightly, but the change was negligible. A slightly stronger inhibition can be found within the NO$_3^-$, which can be ascribed to the fact that the NO$_3^-$ can occupy the active sites of 10% Ag@AgI/V$_I$-BOI

photocatalyst, leading to a decline of photocatalytic activity for TC degradation [38]. As for SO$_4^{2-}$, it can significantly reduce the TC photocatalytic degradation efficiency due to the following reasons. On one hand it inhibits the adsorption of TC molecules on the surface of photocatalyst, on the other it can act as quenchers of h$^+$ and ·OH. Therefore, moderate pretreatment of wastewater is essential for TC
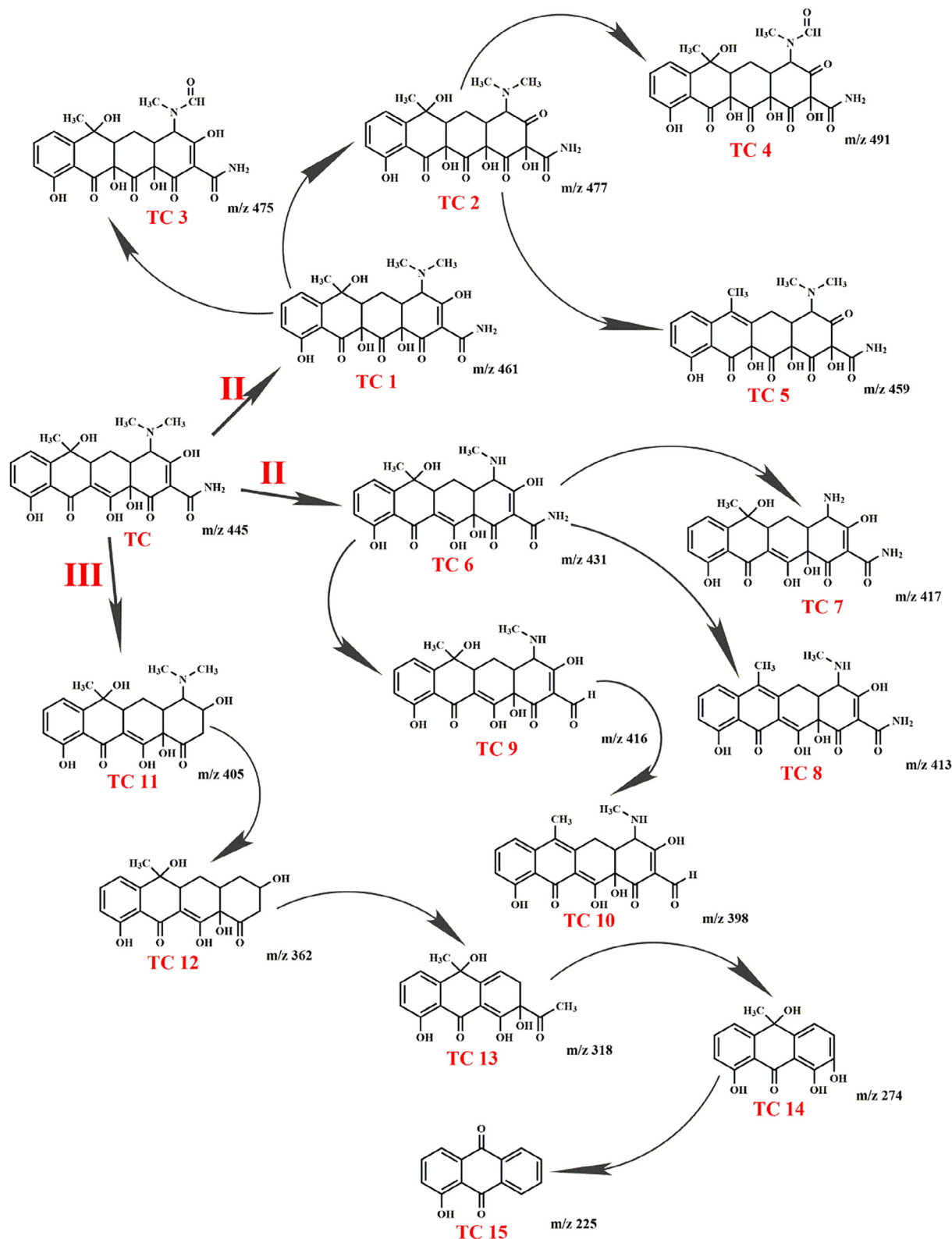
Scheme 1. Suggested photocatalytic degradation pathways of TC.

removal with 10% Ag@AgI/V$_I$-BOI photocatalyst.

3.2.4. The impact of light irradiation conditions

To clarify the impact of light irradiation for the TC degradation efficiency, control experiments were performed by employing a 300 W Xe lamp equipped with or without an optical filter. Fig. 6d shows the degradation efficiency of TC on 10% Ag@AgI/V$_I$-BOI photocatalyst under different irradiation conditions. In the darkness, there was no obvious removal of TC when the suspensions reached the adsorption–desorption equilibrium. But when the 10% Ag@AgI/V$_I$-BOI photocatalyst was exposed to visible light (λ > 420 nm), 86.40% of TC was degraded on 60 min irradiation. Additionally, a higher TC degradation efficiency can be acquired under full spectrum condition (λ > 350 nm) compared with the degradation under visible light irradiation, which can reach to 91.66%. The results are attributed to the enhanced photons energy which are rooted in the short wavelength light source [39]. Thus, the 10% Ag@AgI/V$_I$-BOI photocatalyst has great potentials in practical wastewater treatment since the widely wavelength range of the solar light.

3.3. Possible degradation pathway of TC

The possible degradation pathway of TC was proposed for deepening the understanding of the TC photocatalytic degradation process. The degradation intermediates of TC in the presence of 10% Ag@AgI/V$_I$-BOI photocatalyst were identified by LC-MS/MS. The MS spectra and proposed molecular structure of all products (after 60 min of degradation) are displayed in Fig. S5. According to the detected intermediate products and the related reports, three possible degradation pathways of TC were proposed and illustrated in Scheme 1. Pathway I is mainly the hydroxylation process. First TC was transformed to TC 1 and TC 2 via hydroxylation and multiple hydroxylation reactions, which has been reported in Deng's study [52]. Subsequently, one methyl of the amino group on TC 1 and TC 2 were attacked by ·OH, leading to the formation of compound TC 3 and TC 4, respectively [53]. Besides, TC 2

can change to TC 5 by losing an H$_2$O molecule. Pathway II mainly includes the detachments of *N*-methyl and amino group. This route was through the loss of one *N*-methyl (TC 6) followed by the degradation of TC 6 to TC 7, TC 8 or TC 9 via loss of another *N*-methyl, H$_2$O molecule or amino group, respectively [54]. And the TC 9 can further transform to TC 10 via dehydration reaction. Pathway III is successive fragmentation induced by reactive species. The generation of TC 11 was attributed to the deamidation reaction of TC, while the loss of dimethylamino group on TC 11 formed TC 12. Then the TC 12 was fragmented into TC 13 via dehydroxylation, opening of benzene rings, deethylation and addition reaction. Finally, the TC 13 was changed to TC 14 and TC 15 via deacetylation and oxidation reaction. And similar degradation pathway was proposed in previous investigation by Zhu et al. [55].

Additionally, 3D EEMs can also explain the TC degradation pathway to a certain extent. As revealed in Fig. 7a and b, no apparent changes of fluorescence signals can be seen between the initial TC solution and the solution obtained after 30 min of dark adsorption, implying that TC molecules are hardly degraded or transformed to other products during the adsorption process. When the solution was irradiated by visible light for 10 min, one fluorescence peak located at λ_{ex}/λ_{em} = (340–350 nm)/(500–510 nm) appeared (Fig. 7c), which was ascribed to the generation of humic acid-like organic matters [56]. With the irradiation time was prolonged to 20 and 40 min, the peak was blueshifted to λ_{ex}/λ_{em} = (335–345 nm)/(495–505 nm), and another new peak emerged in the fulvic acids-like fluorescence region of λ_{ex}/λ_{em} = (305–315 nm)/(420–430 nm) [56], as shown in Fig. 7d and e. According to previous reports, a blue shift is related to the break-up of large molecules into smaller fragments and decomposition of condensed aromatic moieties, such as a reduction in the number of aromatic rings and a decrease in the degree of the π-electron system [57]. After 60 min of reaction, the intensity of the peaks was weakened (Fig. 7f), which might be ascribed to a part of intermediates be degraded and evolved to CO$_2$ and H$_2$O. These results are consistent with the proposed TC degradation pathway.
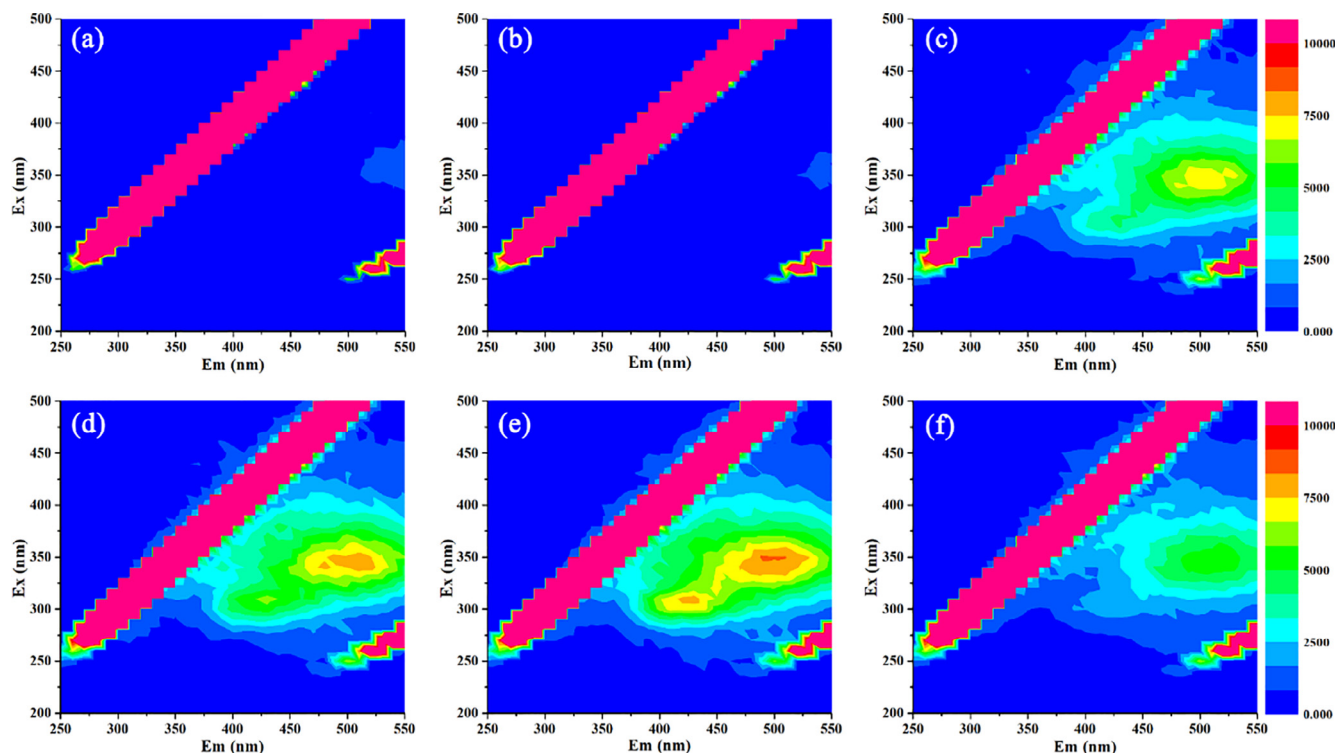

Fig. 7. Three-dimensional excitation-emission matrix fluorescence spectra (3D EEMs) of the TC aqueous solution: (a) taken from the original solution; (b) obtained after 30 min adsorption in dark; and (c-f) collected after visible light irradiation times of 10 min, 20 min, 40 min and 60 min, respectively.

3.4. Mechanism of enhanced photocatalytic activity

The optical properties play an important role in assessing the photocatalytic abilities for photocatalysts. The UV–vis DRS of BiOI, V_I-BOI, Ag@AgI and Ag@AgI/V_I-BOI are presented in Fig. 8a. It can be observed that the absorption edge of V_I-BOI (661 nm) is blue-shifted in comparison to BiOI (682 nm) because the I atoms were replaced by O atoms in their structures. For Ag@AgI, its absorption edge is 446 nm, and the enhancement of visible light absorption at 570 nm is owing to the surface plasmon resonance (SPR) effect of Ag^0 nanoparticles [58]. In contrast to the spectrum of Ag@AgI, the spectrum of Ag@AgI/V_I-BOI presents a broad absorption band between 400 nm and 650 nm that almost contain entire visible light range, ensuring the response of photocatalysts under visible light irradiation.

Moreover, the band gap energy (E_g) of the pure V_I-BOI is calculated from UV–vis DRS taking the following formula and is exhibited in the inset of Fig. 8a [59]:

$$\alpha h v = A (h v - E_g)^{n/2} \tag{3}$$

where α, h, v, A, and E_g are the absorption index, Planck constant, light frequency, a proportionality constant and band gap energy, respectively. Additionally, n relies on the characteristics of the optical transition process in a semiconductor. For V_I-BOI, the value of n is 4 for the indirect transition [34]. Thus, the E_g of V_I-BOI is estimated to be 1.76 eV from the plot of $(\alpha h v)^{1/2}$ *versus* $(h v)$ in the inset of Fig. 8a.

Photoluminescence (PL) emission is considered to be an effective technique for studying the generation, separation, migration and recombination of charge carriers in photocatalysts. Generally, a lower PL intensity indicates a higher photo-excited electron-hole pairs separation efficiency [59]. Fig. 8b reveals the differences on PL spectra of BiOI, V_I-BOI and 10% Ag@AgI/V_I-BOI under an excitation wavelength of 400 nm. Obviously, the V_I-BOI shows reduced PL intensity in

comparison with the pristine BiOI, which signifies that the iodine vacancies result in the inhibition of photo-induced electron-hole pairs recombination. This phenomenon is supported by the result given in previous report that the iodine vacancies can act as traps for photogenerated holes and promote the separation of charge carriers consequently [34,35]. Besides, the 10% Ag@AgI/V_I-BOI presents the lowest PL intensity, suggesting that it owns the highest separation efficiency of photo-induced charge carriers among the prepared photocatalysts.

To further investigate the charge migration and recombination properties, the transient photocurrent responses and EIS analysis were employed. As shown in Fig. 8c, the photocurrent of 10% Ag@AgI/V_I-BOI is much higher than that of BiOI, V_I-BOI and Ag@AgI under visible light irradiation, indicating that the 10% Ag@AgI/V_I-BOI has the fastest separation rate of photo-excited charges. This can be owing to the synergic effect between iodine vacancies, AgI/V_I-BOI heterojunction and Z-scheme bridge metallic Ag^0, which greatly promotes the photo-generated electron-hole pairs separation, inhibits the charges recombination and prolongs the charge carriers lifetime, and thus improving the photocurrent density [41]. Besides, the EIS analysis obtained a similar result. Fig. 8d illustrates the EIS changes of BiOI, V_I-BOI, Ag@AgI and 10% Ag@AgI/V_I-BOI. It is obvious that the relative size of arc is in the order of BiOI > V_I-BOI > Ag@AgI > 10% Ag@AgI/V_I-BOI, which reveals that the 10% Ag@AgI/V_I-BOI expresses a more efficient charge separation and electron transfer ability. Therefore, the photocurrent and EIS results all explicitly prove the excellent photo-electrochemical properties of 10% Ag@AgI/V_I-BOI nanocomposite.

The photocatalytic decomposition of organic contaminants usually happens through the oxidation by h^+, $\cdot OH$ and $\cdot O_2^-$ radicals [60,61]. In order to determine the active species generated during the photocatalytic degradation process of TC on 10% Ag@AgI/V_I-BOI photocatalyst under visible light irradiation, free radicals trapping experiment was performed via adding quenchers. Herein, sodium oxalate
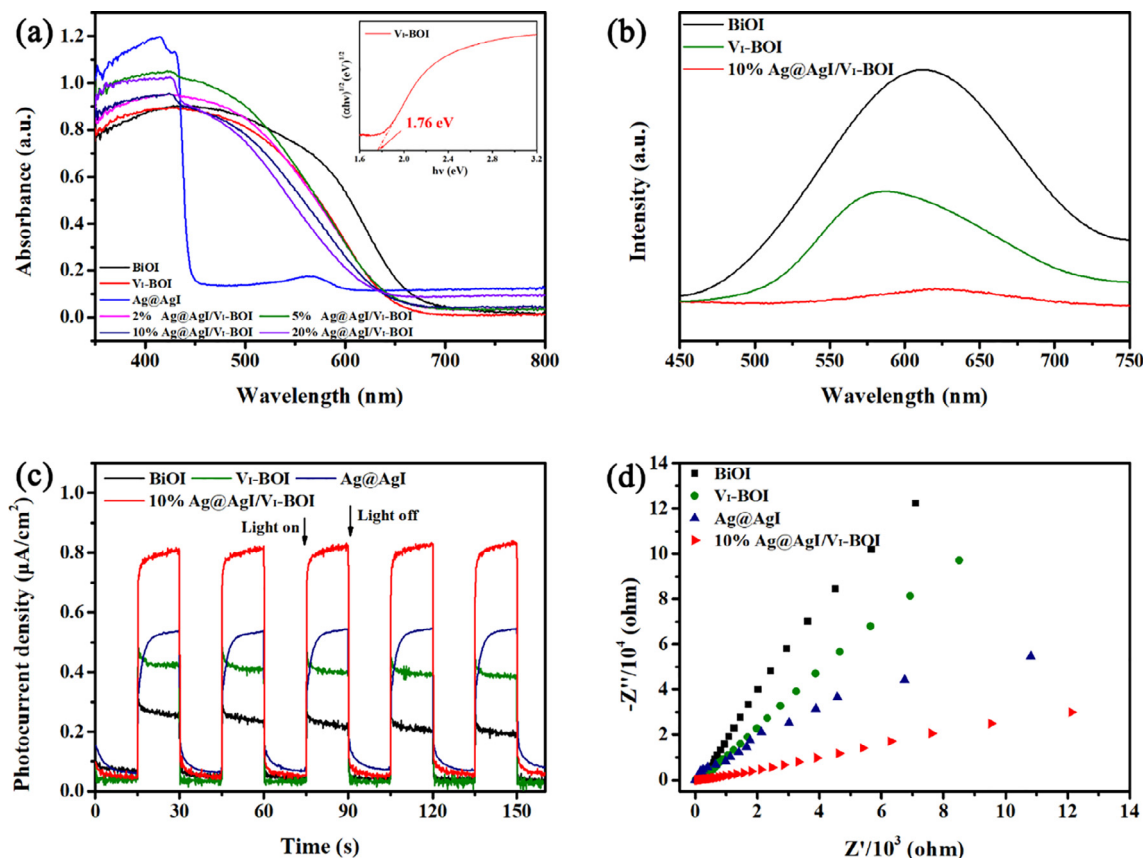

Fig. 8. (a) UV–vis DRS, (b) PL spectra, (c) transient photocurrent responses, and (d) EIS Nyquist plots of the samples.

(Na$_2$C$_2$O$_4$, 10 mM), isopropanol (IPA, 10 mM) and 4-hydroxy-2,2,6,6-tetramethylpiperidinyloxy (TEMPOL, 10 mM) were used as quenchers of photo-generated h$^+$, ·OH and ·O$_2^-$, respectively [62]. As shown in Fig. 9a, the TC degradation was greatly inhibited by adding TEMPOL and Na$_2$C$_2$O$_4$, and weakly suppressed after the addition of IPA. It is suggested that the h$^+$ and ·O$_2^-$ play a dominated role in photocatalytic degradation of TC for 10% Ag@AgI/V$_I$-BOI photocatalyst, while the ·OH plays a secondary role. The active species were further confirmed by ESR signals analysis. Fig. 9b shows the ESR signals of ·O$_2^-$ trapped by DMPO in the presence of 10% Ag@AgI/V$_I$-BOI photocatalyst. Obviously, there were no signals in dark, but intensive characteristic signals were detected under visible light irradiation. Similarly, as exhibited in Fig. 9c, the characteristic signals of ·OH can be ignored in dark while also can be found under visible light irradiation. The ESR results demonstrate that the ·O$_2^-$ and ·OH is generated during the photocatalytic degradation process, which are in coincidence with the free radicals trapping experiments.

To explain the mechanism of enhanced photocatalytic activity, the valence band (VB) and conduction band (CB) potentials of V$_I$-BOI and AgI should be initially confirmed. For V$_I$-BOI, the potential of VB (E_{VB}) is estimated to be 2.44 eV through VB-XPS in Fig. S6, and the potential of CB (E_{CB}) is calculated to be 0.68 eV by the following formula [52]:

$$E_{CB} = E_{VB} - E_g \tag{4}$$

where E_g is evaluated to be 1.76 eV from the above investigation. As for AgI, on the basis of our previous reports [46,49], the E_{VB}, E_{CB} and E_g are confirmed to be 2.35, −0.42 and 2.77 eV, respectively. Based on the experimental data and theoretical analysis above mentioned, a Z-scheme mechanism for the TC photocatalytic degradation over Ag@AgI/V$_I$-BOI nanocomposite is proposed, and illustrated in Scheme 2. It can be observed that both the V$_I$-BOI and AgI can be excited to generate electrons and holes under visible light irradiation. According to conventional p-n heterojunction, the photo-excited electrons on the VB of AgI would migrate to the VB of V$_I$-BOI and the photo-excited holes on the CB of V$_I$-BOI would transfer to the CB of AgI [63]. But, the electrons on the CB of V$_I$-BOI cannot react with O$_2$ to generate ·O$_2^-$ as the CB potential of V$_I$-BOI (0.68 eV vs NHE) is more positive than the reduction potential of O$_2$/·O$_2^-$ (−0.33 eV vs NHE) and the holes on the VB of AgI cannot react with OH$^-$ to form ·OH because the VB potential of AgI (2.35 eV vs NHE) is more negative than the oxidation potential of OH$^-$/·OH (2.40 eV vs NHE) [64]. However, the ·OH and ·O$_2^-$ radicals are confirmed to be produced and participated in this photocatalytic degradation process from the radicals trapping experiment and ESR analysis. Besides, the iodine vacancies can act as traps for holes and the metallic Ag^0 can serve as mediators for electrons transfer [35,41], so the Z-scheme mechanism is more reasonable to explain the enhanced photocatalytic activity. In this Z-scheme photocatalytic system, the photo-generated holes on the VB of V$_I$-BOI are firstly trapped by iodine vacancies and then migrate to the surface of V$_I$-BOI, which significantly accelerate the transportation of photo-generated holes and restrain the recombination of photo-induced electron-hole pairs over V$_I$-BOI. The holes can directly react with TC, or react with H$_2$O to form ·OH and degrade TC subsequently owing to the VB potential of V$_I$-BOI (2.44 eV vs NHE) being more positive than the oxidation potential of OH$^-$/·OH (2.40 eV vs NHE). Moreover, the electrons on the CB of V$_I$-BOI easily flow into Ag and transfer to the VB of AgI, recombining with the remainder holes on the VB of AgI. It is faster than the recombination rate of holes and electrons for AgI itself, which greatly promote the separation of the charges over AgI. Meanwhile, the photo-excited electrons in the CB of AgI can react with dissolved O$_2$ to produce ·O$_2^-$ for TC degradation due to its negative CB potential (−0.42 eV vs NHE). Therefore, the photocatalytic activity of Ag@AgI/V$_I$-BOI is improved remarkably.

3.5. Recyclability and stability

To explore the recyclability and stability of the 10% Ag@AgI/V$_I$-BOI photocatalyst for the photocatalytic degradation of TC, the 10% Ag@AgI/V$_I$-BOI powders were reused four times under the same

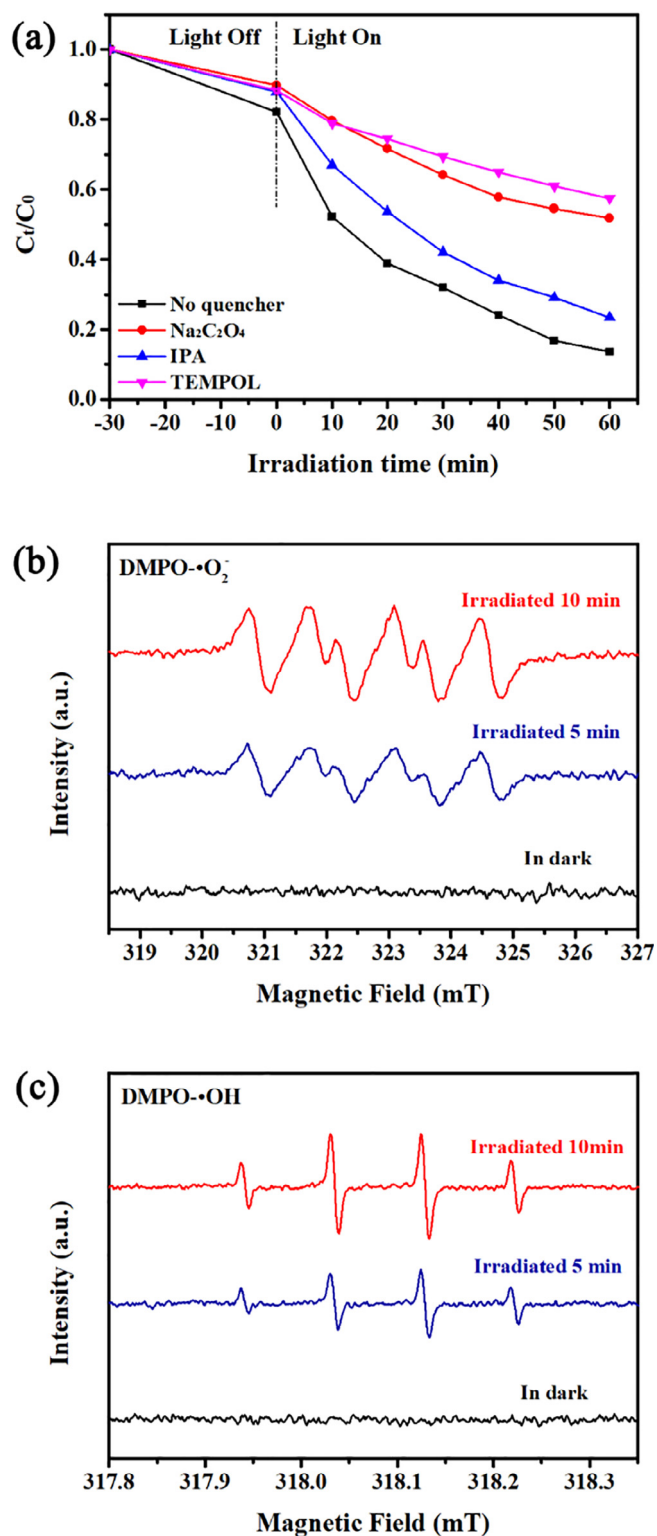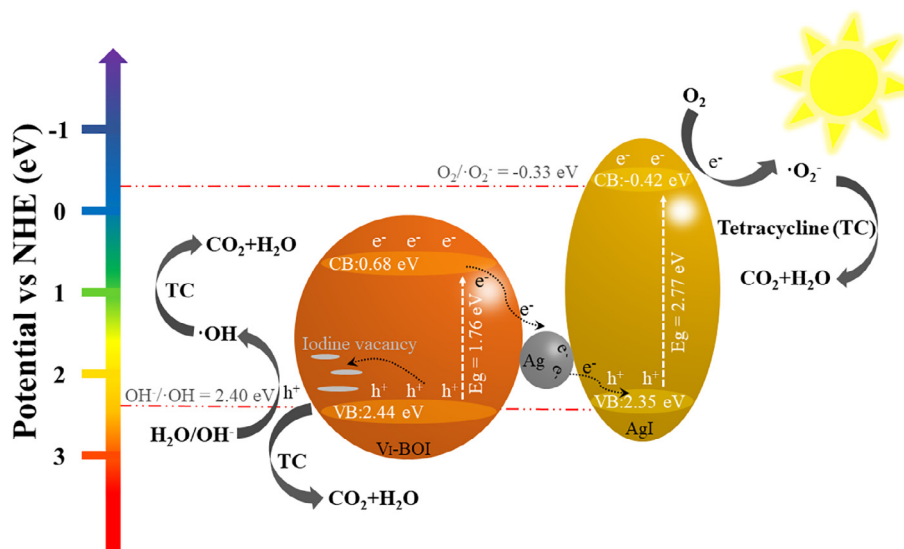**Fig. 9.** (a) Photocatalytic degradation of TC under visible light irradiation over 10% Ag@AgI/V$_I$-BOI photocatalyst with different quenchers; DMPO spin-trapping ESR spectra of 10% Ag@AgI/V$_I$-BOI sample: (b) DMPO-·O$_2^-$ and (b) DMPO-·OH.

Scheme 2. The proposed mechanism for the enhancement of photocatalytic activity.

reaction conditions and the results are presented in Fig. 10a. After four cycles, the 10% Ag@AgI/V_I-BOI sample still holds an excellent photocatalytic activity for the degradation of TC and the photocatalytic degradation efficiency is 81.17%, only decreases 5.23%. The HRTEM image (Fig. 10b), XRD pattern (Fig. 10c) and UV–vis DRS (Fig. 10d) of the used photocatalyst (four times) indicate that its structure, phase and optical properties keep unchanged after the photocatalytic reactions for four times. Therefore, the 10% Ag@AgI/V_I-BOI photocatalyst possesses

an excellent recyclability and stability for the photocatalytic degradation of TC under visible light irradiation, which have great potential in future practical applications.

4. Conclusions

In summary, a novel Z-scheme heterojunction photocatalyst of Ag@AgI/defective BiOI (Ag@AgI/V_I-BOI) was developed and applied
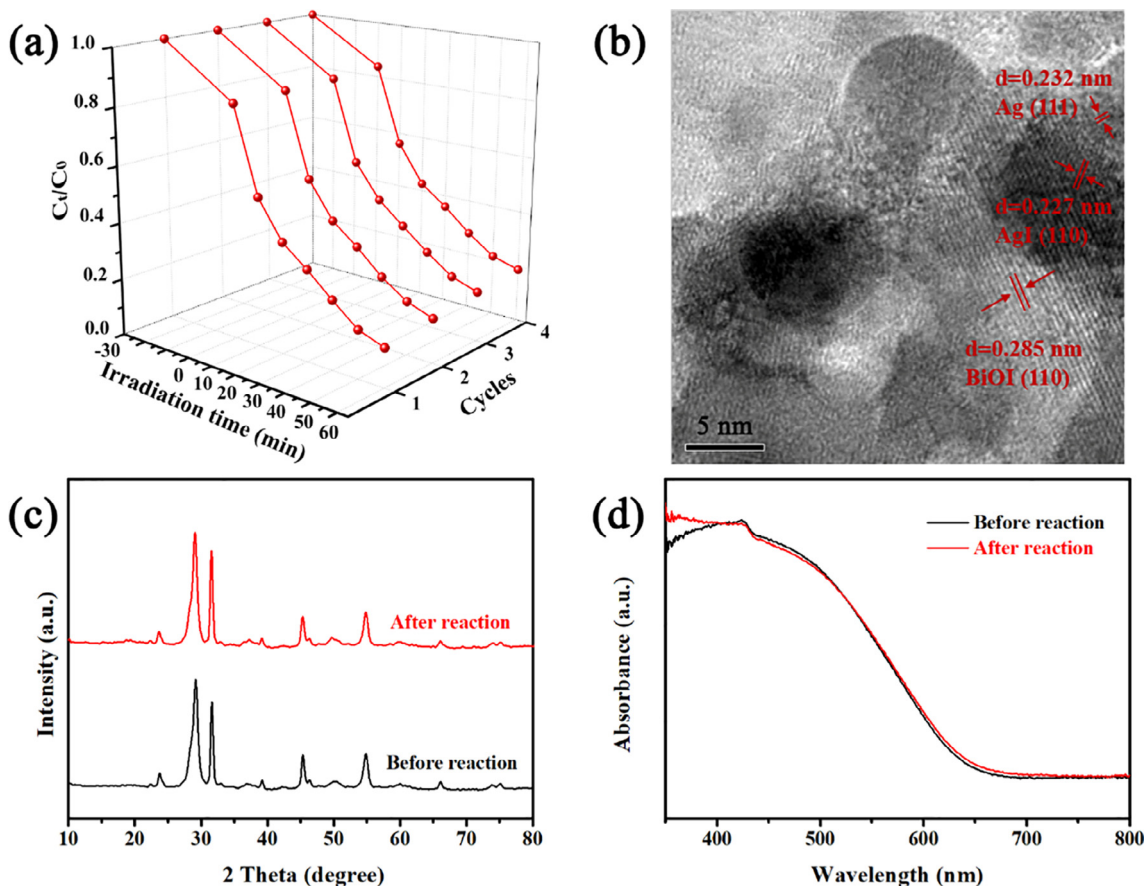

Fig. 10. (a) Cycling runs for photocatalytic degradation of TC in the presence of 10% Ag@AgI/V_I-BOI; (b) HRTEM image of the used 10% Ag@AgI/V_I-BOI; (c) XRD patterns and (d) UV–vis DRS of the 10% Ag@AgI/V_I-BOI before and after the photocatalytic degradation process.

to TC elimination. The fabricated 10% Ag@AgI/V$_I$-BOI photocatalyst possessed the optimum photocatalytic efficiency for the degradation of TC under visible light irradiation ($\lambda > 420$ nm), which was better than that of BiOI, V$_I$-BOI and Ag@AgI. Three possible decomposition pathways of the degradation process were proposed based on the LC/MS-MS and 3D EEMs results. Active species trapping experiments and ESR signals revealed that $\cdot O_2^-$, h$^+$ and $\cdot OH$ were the active species involved in TC photocatalytic degradation process. It is worth pointing out that the synergetic effect among iodine vacancies, AgI/V$_I$-BOI heterojunction and metallic Ag^0 should contribute to the improved photocatalytic performance towards TC removal because the iodine vacancies can act as traps for holes and the metallic Ag^0 can serve as mediators for electrons transfer. This work highlights the indispensable role of iodine vacancies and Z-scheme heterojunction in the enhancement of photocatalytic performance and provides a new insight to the design of novel photocatalysts for practical wastewater treatment.

Acknowledgments

Appendix A. Supplementary data

Supplementary data associated with this article can be found, in the online version, at http://dx.doi.org/10.1016/j.cej.2018.05.093.

References

[1] G. Zeng, C. Zhang, D. Huang, C. Lai, L. Tang, Y. Zhou, P. Xu, H. Wang, L. Qin, M. Cheng, Practical and regenerable electrochemical aptasensor based on nanoporous gold and thymine-Hg^{2+}-thymine base pairs for Hg^{2+} detection, Biosens. Bioelectron. 90 (2017) 542–548.

[2] C. Zhang, C. Lai, G. Zeng, D. Huang, L. Tang, C. Yang, Y. Zhou, L. Qin, M. Cheng, Nanoporous Au-based chronocoulometric aptasensor for amplified detection of Pb^{2+} using DNAzyme modified with Au nanoparticles, Biosens. Bioelectron. 81 (2016) 61–67.

[3] J. Wan, G. Zeng, D. Huang, L. Hu, P. Xu, C. Huang, R. Deng, W. Xue, C. Lai, C. Zhou, K. Zheng, X. Ren, X. Gong, Rhamnolipid stabilized nano-chlorapatite: synthesis and enhancement effect on Pb-and Cd-immobilization in polluted sediment, J. Hazard. Mater. 343 (2018) 332–339.

[4] W. Tang, G. Zeng, J. Gong, J. Liang, P. Xu, C. Zhang, B. Huang, Impact of humic/fulvic acid on the removal of heavy metals from aqueous solutions using nanomaterials: a review, Sci. Total Environ. 468–469 (2014) 1014–1027.

[5] Y. Zhang, G. Zeng, L. Tang, J. Chen, Y. Zhu, X. He, Y. He, Electrochemical sensor based on electrodeposited graphene-Au modified electrode and nanoAu carrier amplified signal strategy for attomolar mercury detection, Anal. Chem. 87 (2015) 989–996.

[6] D. Huang, W. Xue, G. Zeng, J. Wan, G. Chen, C. Huang, C. Zhang, M. Cheng, P. Xu, Immobilization of Cd in river sediments by sodium alginate modified nanoscale zero-valent iron: impact on enzyme activities and microbial community diversity, Water Res. 106 (2016) 15–25.

[7] X. Gong, D. Huang, Y. Liu, G. Zeng, R. Wang, J. Wan, C. Zhang, M. Cheng, X. Qin, W. Xue, Stabilized nanoscale zerovalent iron mediated cadmium accumulation and oxidative damage of *Boehmeria nivea* (L.) gaudich cultivated in cadmium contaminated sediments, Environ. Sci. Technol. 51 (2017) 11308–11316.

[8] X. Tan, Y. Liu, G. Zeng, X. Wang, X. Hu, Y. Gu, Z. Yang, Application of biochar for the removal of pollutants from aqueous solutions, Chemosphere 125 (2015) 70–85.

[9] P. Xu, G. Zeng, D. Huang, C. Feng, S. Hu, M. Zhao, C. Lai, Z. Wei, C. Huang, G. Xie, Z. Liu, Use of iron oxide nanomaterials in wastewater treatment: a review, Sci. Total Environ. 424 (2012) 1–10.

[10] J. Deng, X. Zhang, G. Zeng, J. Gong, Q. Niu, J. Liang, Simultaneous removal of Cd (II) and ionic dyes from aqueous solution using magnetic graphene oxide nanocomposite as an adsorbent, Chem. Eng. J. 226 (2013) 189–200.

[11] F. Long, J. Gong, G. Zeng, L. Chen, X. Wang, J. Deng, Q. Niu, H. Zhang, X. Zhang, Removal of phosphate from aqueous solution by magnetic Fe-Zr binary oxide, Chem. Eng. J. 171 (2011) 448–455.

[12] D. Huang, X. Wang, C. Zhang, G. Zeng, Z. Peng, J. Zhou, M. Cheng, R. Wang, Z. Hu, X. Qin, Sorptive removal of ionizable antibiotic sulfamethazine from aqueous solution by graphene oxide-coated biochar nanocomposites: influencing factors and mechanism, Chemosphere 186 (2017) 414–421.

[13] C. Zhang, C. Lai, G. Zeng, D. Huang, C. Yang, Y. Wang, Y. Zhou, M. Cheng, Efficacy of carbonaceous nanocomposites for sorbing ionizable antibiotic sulfamethazine from aqueous solution, Water Res. 95 (2016) 103–112.

[14] J. Gong, B. Wang, G. Zeng, C. Yang, C. Niu, Q. Niu, W. Zhou, Y. Liang, Removal of cationic dyes from aqueous solution using magnetic multi-wall carbon nanotube nanocomposite as adsorbent, J. Hazard. Mater. 164 (2009) 1517–1522.

[15] P. Xu, G. Zeng, D. Huang, C. Lai, M. Zhao, Z. Wei, N. Li, C. Huang, G. Xie, Adsorption of Pb(II) by iron oxide nanoparticles immobilized *Phanerochaete chrysosporium*: equilibrium, kinetic, thermodynamic and mechanisms analysis, Chem. Eng. J. 203 (2012) 423–431.

[16] D. Huang, L. Liu, G. Zeng, P. Xu, C. Huang, L. Deng, R. Wang, J. Wan, The effects of rice straw biochar on indigenous microbial community and enzymes activity in heavy metal-contaminated sediment, Chemosphere 174 (2017) 545–553.

[17] M. Cheng, G. Zeng, D. Huang, C. Lai, P. Xu, C. Zhang, Y. Liu, Hydroxyl radicals based advanced oxidation processes (AOPs) for remediation of soils contaminated with organic compounds: a review, Chem. Eng. J. 284 (2016) 582–598.

[18] X. Ren, G. Zeng, L. Tang, J. Wang, J. Wan, Y. Liu, J. Yu, H. Yi, S. Ye, R. Deng, Sorption, transport and biodegradation-an insight into bioavailability of persistent organic pollutants in soil, Sci. Total Environ. 610–611 (2018) 1154–1163.

[19] H. Wu, C. Lai, G. Zeng, J. Liang, J. Chen, J. Xu, J. Dai, X. Li, J. Liu, M. Chen, L. Lu, L. Hu, J. Wan, The interactions of composting and biochar and their implications for soil amendment and pollution remediation: a review, Crit. Rev. Biotechnol. 37 (2016) 754–764.

[20] D. Huang, C. Hu, G. Zeng, M. Cheng, P. Xu, X. Gong, R. Wang, W. Xue, Combination of fenton processes and biotreatment for wastewater treatment and soil remediation, Sci. Total Environ. 574 (2017) 1599–1610.

[21] J. Liang, Z. Yang, L. Tang, G. Zeng, M. Yu, X. Li, H. Wu, Y. Qian, X. Li, Y. Luo, Changes in heavy metal mobility and availability from contaminated wetland soil remediated with combined biochar-compost, Chemosphere 181 (2017) 281–288.

[22] M. Chen, P. Xu, G. Zeng, C. Yang, D. Huang, J. Zhang, Bioremediation of soils contaminated with polycyclic aromatic hydrocarbons, petroleum, pesticides, chlorophenols and heavy metals by composting: applications, microbes and future research needs, Biotechnol. Adv. 33 (2015) 745–755.

[23] D. Huang, R. Wang, Y. Liu, G. Zeng, C. Lai, P. Xu, B. Lu, J. Xu, C. Wang, C. Huang, Application of molecularly imprinted polymers in wastewater treatment: a review, Environ. Sci. Pollut. Res. Int. 22 (2015) 963–977.

[24] C. Lai, M. Wang, G. Zeng, Y. Liu, D. Huang, C. Zhang, R. Wang, P. Xu, M. Cheng, C. Huang, H. Wu, L. Qin, Synthesis of surface molecular imprinted TiO$_2$/graphene photocatalyst and its highly efficient photocatalytic degradation of target pollutant under visible light irradiation, Appl. Surf. Sci. 390 (2016) 368–376.

[25] L. Tang, J. Wang, G. Zeng, Y. Liu, Y. Deng, Y. Zhou, J. Tang, J. Wang, Z. Guo, Enhanced photocatalytic degradation of norfloxacin in aqueous Bi$_2$WO$_6$ dispersions containing nonionic surfactant under visible light irradiation, J. Hazard. Mater. 306 (2016) 295–304.

[26] C. Zhou, C. Lai, P. Xu, G. Zeng, D. Huang, C. Zhang, M. Cheng, L. Hu, J. Wan, Y. Liu, W. Xiong, Y. Deng, M. Wen, In situ grown AgI/Bi$_{12}$O$_{17}$Cl$_2$ heterojunction photocatalysts for visible light degradation of sulfamethazine: efficiency, pathway, and mechanism, ACS Sustain. Chem. Eng. 6 (2018) 4174–4184.

[27] Y. Yang, C. Zhang, C. Lai, G. Zeng, D. Huang, M. Cheng, J. Wang, F. Chen, C. Zhou, W. Xiong, BiOX (X = Cl, Br, I) photocatalytic nanomaterials: applications for fuels and environmental management, Adv. Colloid Interface Sci. (2017), http://dx.doi.org/10.1016/j.cis.2018.03.004.

[28] X. Wen, C. Niu, L. Zhang, G. Zeng, Fabrication of SnO$_2$ Nanopaticles/BiOI n-p heterostructure for wider spectrum visible-light photocatalytic degradation of antibiotic oxytetracycline hydrochloride, ACS Sustain. Chem. Eng. 5 (2017) 5134–5147.

[29] X. Wen, C. Niu, L. Zhang, G. Zeng, Novel p-n heterojunction BiOI/CeO$_2$ photocatalyst for wider spectrum visible-light photocatalytic degradation of refractory pollutants, Dalton Trans. 46 (2017) 4982–4993.

[30] X. Wen, C. Niu, L. Zhang, C. Liang, G. Zeng, An in depth mechanism insight of the degradation of multiple refractory pollutants via a novel SrTiO$_3$/BiOI heterojunction photocatalysts, J. Catal. 356 (2017) 283–299.

[31] H. Li, J. Shang, Z. Ai, L. Zhang, Efficient visible light nitrogen fixation with BiOBr nanosheets of oxygen vacancies on the exposed 001 facets, J. Am. Chem. Soc. 137 (2015) 6393–6399.

[32] H. Li, J. Li, Z. Ai, F. Jia, L. Zhang, Oxygen vacancy-mediated photocatalysis of BiOCl: reactivity, selectivity, and perspectives, Angew. Chem. Int. Ed. Eng. 57 (2018) 122–138.

[33] M. Long, P. Hu, H. Wu, Y. Chen, B. Tan, W. Cai, Understanding the composition and electronic structure dependent photocatalytic performance of bismuth oxyiodides, J. Mater. Chem. A 3 (2015) 5592–5598.

[34] Y. Guan, S. Wang, X. Wang, C. Sun, Y. Wang, Z. Ling, Solvothermal method coupled with thermal decomposition for synthesis of non-stoichiometric BiO$_{1.18}$I$_{0.64}$ with excellent photocatalytic activity, RSC Adv. 6 (2016) 2641–2650.

[35] S. Cui, G. Shan, L. Zhu, Solvothermal synthesis of I-deficient BiOI thin film with distinct photocatalytic activity and durability under simulated sunlight, Appl. Catal., B 219 (2017) 249–258.

[36] J. Li, Y. Yu, L. Zhang, Bismuth oxyhalide nanomaterials: layered structures meet photocatalysis, Nanoscale 6 (2014) 8473–8488.

[37] X. Chen, R. Li, X. Pan, X. Huang, Z. Yi, Fabrication of In$_2$O$_3$-Ag-Ag$_3$PO$_4$ composites with Z-scheme configuration for photocatalytic ethylene degradation under visible

light irradiation, Chem. Eng. J. 320 (2017) 644–652.

[38] F. Chen, Q. Yang, Y. Wang, J. Zhao, D. Wang, X. Li, Z. Guo, H. Wang, Y. Deng, C. Niu, G. Zeng, Novel ternary heterojunction photcocatalyst of Ag nanoparticles and g-C₃N₄ nanosheets co-modified BiVO₄ for wider spectrum visible-light photocatalytic degradation of refractory pollutant, Appl. Catal., B 205 (2017) 133–147.

[39] Y. Deng, L. Tang, G. Zeng, C. Feng, H. Dong, J. Wang, H. Feng, Y. Liu, Y. Zhou, Y. Pang, Plasmonic resonance excited dual Z-scheme BiVO₄/Ag/Cu₂O nanocomposite: synthesis and mechanism for enhanced photocatalytic performance in recalcitrant antibiotic degradation, Environ. Sci. Nano 4 (2017) 1494–1511.

[40] H. Guo, C. Niu, X. Wen, L. Zhang, C. Liang, X. Zhang, D. Guan, N. Tang, G. Zeng, Construction of highly efficient and stable ternary AgBr/Ag/PbBiO₂Br Z-scheme photocatalyst under visible light irradiation: performance and mechanism insight, J. Colloid Interface Sci. 513 (2017) 852–865.

[41] L. Ye, J. Liu, C. Gong, L. Tian, T. Peng, L. Zan, Two different roles of metallic Ag on Ag/AgX/BiOX (X = Cl, Br) visible light photocatalysts: surface plasmon resonance and Z-Scheme bridge, ACS Catal. 2 (2012) 1677–1683.

[42] X. Wen, C. Niu, D. Huang, L. Zhang, C. Liang, G. Zeng, Study of the photocatalytic degradation pathway of norfloxacin and mineralization activity using a novel ternary Ag/AgCl-CeO₂ photocatalyst, J. Catal. 355 (2017) 73–86.

[43] D. Xia, T. An, G. Li, W. Wang, H. Zhao, P.K. Wong, Synergistic photocatalytic inactivation mechanisms of bacteria by graphene sheets grafted plasmonic Ag-AgX (X = Cl, Br, I) composite photocatalyst under visible light irradiation, Water Res. 99 (2016) 149–161.

[44] S. Ning, H. Lin, Y. Tong, X. Zhang, Q. Lin, Y. Zhang, J. Long, X. Wang, Dual couples Bi metal depositing and Ag@AgI islanding on BiOI 3D architectures for synergistic bactericidal mechanism of *E. coli* under visible light, Appl. Catal., B 204 (2017) 1–10.

[45] L. Chen, D. Jiang, T. He, Z. Wu, M. Chen, In-situ ion exchange synthesis of hierarchical AgI/BiOI microsphere photocatalyst with enhanced photocatalytic properties, CrystEngComm 15 (2013) 7556.

[46] F. Chen, Q. Yang, J. Sun, F. Yao, S. Wang, Y. Wang, X. Wang, X. Li, C. Niu, D. Wang, G. Zeng, Enhanced photocatalytic degradation of tetracycline by AgI/BiVO₄ heterojunction under visible-light irradiation: mineralization efficiency and mechanism, ACS Appl. Mater. Interfaces 8 (2016) 32887–32900.

[47] L. Ye, X. Jin, X. Ji, C. Liu, Y. Su, H. Xie, C. Liu, Facet-dependent photocatalytic reduction of CO₂ on BiOI nanosheets, Chem. Eng. J. 291 (2016) 39–46.

[48] M. Cui, J. Yu, H. Lin, Y. Wu, L. Zhao, Y. He, In-situ preparation of Z-scheme AgI/Bi₅O₇I hybrid and its excellent photocatalytic activity, Appl. Surf. Sci. 387 (2016) 912–920.

[49] X. Wen, C. Niu, M. Ruan, L. Zhang, G. Zeng, AgI nanoparticles-decorated CeO₂ microsheets photocatalyst for the degradation of organic dye and tetracycline under visible-light irradiation, J. Colloid Interface Sci. 497 (2017) 368–377.

[50] R. Hao, X. Xiao, X. Zuo, J. Nan, W. Zhang, Efficient adsorption and visible-light photocatalytic degradation of tetracycline hydrochloride using mesoporous BiOI microspheres, J. Hazard. Mater. 209–210 (2012) 137–145.

[51] X. Liu, P. Lv, G. Yao, C. Ma, P. Huo, Y. Yan, Microwave-assisted synthesis of selective degradation photocatalyst by surface molecular imprinting method for the

degradation of tetracycline onto Cl-TiO₂, Chem. Eng. J. 217 (2013) 398–406.

[52] Y. Deng, L. Tang, G. Zeng, J. Wang, Y. Zhou, J. Wang, J. Tang, L. Wang, C. Feng, Facile fabrication of mediator-free Z-scheme photocatalyst of phosphorous-doped ultrathin graphitic carbon nitride nanosheets and bismuth vanadate composites with enhanced tetracycline degradation under visible light, J. Colloid Interface Sci. 509 (2018) 219–234.

[53] N. Barhoumi, H. Olvera-Vargas, N. Oturan, D. Huguenot, A. Gadri, S. Ammar, E. Brillas, M.A. Oturan, Kinetics of oxidative degradation/mineralization pathways of the antibiotic tetracycline by the novel heterogeneous electro-Fenton process with solid catalyst chalcopyrite, Appl. Catal., B 209 (2017) 637–647.

[54] S. Li, J. Hu, Photolytic and photocatalytic degradation of tetracycline: effect of humic acid on degradation kinetics and mechanisms, J. Hazard. Mater. 318 (2016) 134–144.

[55] Z. Zhu, Y. Yu, H. Huang, X. Yao, H. Dong, Z. Liu, Y. Yan, C. Li, P. Huo, Microwave-hydrothermal synthesis of a novel, recyclable and stable photocatalytic nanoreactor for recognition and degradation of tetracycline, Catal. Sci. Technol. 7 (2017) 4092–4104.

[56] W. Chen, P. Westerhoff, J. Leenheer, K. Booksh, Fluorescence excitation-emission matrix regional integration to quantify spectra for dissolved organic matter, Environ. Sci. Technol. 37 (2003) 5701.

[57] Z. Wang, Z. Wu, S. Tang, Characterization of dissolved organic matter in a submerged membrane bioreactor by using three-dimensional excitation and emission matrix fluorescence spectroscopy, Water Res. 43 (2009) 1533–1540.

[58] H. Cheng, W. Wang, B. Huang, Z. Wang, J. Zhan, X. Qin, X. Zhang, Y. Dai, Tailoring AgI nanoparticles for the assembly of AgI/BiOI hierarchical hybrids with size-dependent photocatalytic activities, J. Mater. Chem. A 1 (2013) 7131.

[59] C. Zhou, C. Lai, D. Huang, G. Zeng, C. Zhang, M. Cheng, L. Hu, J. Wan, W. Xiong, M. Wen, X. Wen, L. Qin, Highly porous carbon nitride by supramolecular preassembly of monomers for photocatalytic removal of sulfamethazine under visible light driven, Appl. Catal., B 220 (2018) 202–210.

[60] J. Wang, L. Tang, G. Zeng, Y. Deng, Y. Liu, L. Wang, Y. Zhou, Z. Guo, J. Wang, C. Zhang, Atomic scale g-C₃N₄/Bi₂WO₆ 2D/2D heterojunction with enhanced photocatalytic degradation of ibuprofen under visible light irradiation, Appl. Catal., B 209 (2017) 285–294.

[61] L. Jiang, L. Yuan, G. Zeng, Z. Wu, J. Liang, X. Chen, L. Leng, H. Wang, H. Wang, Metal-free efficient photocatalyst for stable visible-light photocatalytic degradation of refractory pollutant, Appl. Catal., B 221 (2018) 715–725.

[62] W. Wang, Y. Yu, T. An, G. Li, H.Y. Yip, J.C. Yu, P.K. Wong, Visible-light-driven photocatalytic inactivation of *E. coli K-12* by bismuth vanadate nanotubes: bactericidal performance and mechanism, Environ. Sci. Technol. 46 (2012) 4599–4606.

[63] H. Cheng, B. Huang, Y. Dai, X. Qin, X. Zhang, One-step synthesis of the nanostructured AgI/BiOI composites with highly enhanced visible-light photocatalytic performances, Langmuir 26 (2010) 6618–6624.

[64] W. Jo, T. Natarajan, Influence of TiO₂ morphology on the photocatalytic efficiency of direct Z-scheme g-C₃N₄/TiO₂ photocatalysts for isoniazid degradation, Chem. Eng. J. 281 (2015) 549–565.